CP845, *Shock Compression of Condensed Matter - 2005,*
edited by M. D. Furnish, M. Elert, T. P. Russell, and C. T. White

MATERIALS RESPONSE UNDER EXTREME CONDITIONS

B.A. Remington[1], J. Hawreliak[1], K.T. Lorenz[1], H.E. Lorenzana[1], J.M. McNaney[1], S.M. Pollaine[1], D.C. Swift[2], B. Yaakobi[3]

[1]*Lawrence Livermore National Laboratory, Livermore CA 94550*
[2]*Los Alamos National Laboratory, Los Alamos NM 87545*
[3]*Laboratory for Laser Energetics, University of Rochester, Rochester, New York 14623*

Abstract. Solid state experiments at extreme pressures (0.1 - 1 Mbar) and strain rates (10^6–10^8 s^{-1}) are being developed on high-energy laser facilities. The goal is a capability to test constitutive models for high-pressure, solid-state strength of materials. Relevant constitutive models are discussed, and our progress in developing a ramped-pressure, shockless drive is given. Designs to test the constitutive models with experiments measuring perturbation growth due to the Rayleigh-Taylor instability in solid-state samples are presented. Results from dynamic diffraction and EXAFS lattice diagnostics are given, showing that compression, phase, and temperature can be inferred on sub-nsec time scales.

Keywords: high pressure strength, constitutive models, Rayleigh-Taylor instability, laser experiments, dynamic diffraction, dynamic EXAFS, phase transformation.
PACS: 61.10.-I, 61.10.Ht, 62.20.-x, 62.20.Fe, 62.50.+p., 81.30.-t, 81.70.Bt, 83.10.Gr, 83.10.Tv

INTRODUCTION

New regimes of materials science at extreme pressures, compressions, and strain rates are being pursued on high energy density facilities, such as lasers, [1,2] Z-pinch facilities, [3,4] and gas guns. [5] One of our goals in this area, aimed at the National Ignition Facility laser (NIF), [6] is to experimentally test models of high pressure, high strain rate material strength at pressures P >> 100 GPa (1 Mbar). We review here aspects of our progress towards achieving this challenging goal.

CONSTITUTIVE MODELS

We begin with a discussion of constitutive models for material strength at high pressures and strain rates ($\dot{\varepsilon}$). [7-11] The Steinberg-Guinan (S-G) model, [8] a first order Taylor expansion in pressure (P) and temperature (T), is written

$$\sigma = \sigma_0 f(\varepsilon)\left[1+\left(\frac{G_P'}{G_0}\right)\frac{P}{\eta^{1/3}}+\left(\frac{G_T'}{G_0}\right)(T-300)\right] . \quad (1)$$

Here, σ_0, ε, $f(\varepsilon)=[1+\beta(\varepsilon_i+\varepsilon)]^n$, and $\eta = \rho/\rho^0$ represent the ambient strength, plastic strain, work hardening factor, and compression, resp. This model applies only to high strain rate, $\dot{\varepsilon} > \sim 10^5$ s^{-1}, and is independent of strain rate. The Steinberg-Lund model [1,9] (S-L) is given as:

$$\sigma = [\sigma_T + \sigma_A f(\varepsilon)]\frac{G}{G_0} , \quad (2a)$$

$$\hat{\sigma} \approx \hat{\sigma}_T + \hat{\sigma}_A f(\varepsilon) , \quad (2b)$$

where σ, σ_T, σ_A, and $f(\varepsilon)$ are yield strength, the thermal and athermal components of strength, and the work hardening factor, resp. The nominal S-L

model requires that (1) $\sigma_A f(\varepsilon)$ not exceed an upper limit, σ^*_{max}, and (2) σ_T not exceed a cap, typically taken as the Peierls stress, σ_P. If this cap on σ_T is removed, we will call this modified case the S-L_1 model. To put the S-L model into dimensionless form, we write $(\hat{\sigma}, \hat{\sigma}_{T,A}) = (\sigma/G, \sigma_{T,A}/G_0)$, (see Eq. 2b) where G_0 and G correspond to the shear modulus at ambient and high - (P,T) conditions. Starting with Orowan's equation, $\dot{\varepsilon} = \rho_m b \bar{v}_{disloc}$, where $\rho_m(cm^{-2})$ and $\bar{v}_{disloc}$ correspond to mobile dislocation density and average dislocation velocity, we can relate σ_T to the strain rate. The form we write down differs slightly from the nominal Hoge-Mukherjee (H-M) model [7], and is given by

$$\dot{\varepsilon} = \frac{\rho_m b^2}{\frac{1}{\alpha \nu_{De}} \exp\left\{\frac{2U_k}{kT}\left[1-\left(\frac{\sigma_T}{\sigma_P}\right)^p\right]^q\right\} + \left(\frac{D^*}{\sigma_T}\right)^m} \quad (3)$$

where p and q represent barrier shape parameters, m is the power of the phonon drag term, D* is the phonon drag coefficient (dimensionally different from that in nominal S-L or H-M, except when m=1), and no artificial cap on σ_T is imposed. We will refer to this model as H-M*. The nominal form of H-M is recovered if p=1, q=2, and m=1. When σ_T resulting from Eq. 3 is inserted into Eq. 2a, we will call this the S-L_2 model. Nominal S-L is recovered with (p, q, m) = (1, 2, 1), and the cap imposed on σ_T, as discussed above.

For the following discussion, we consider just the thermal activation component of Eq. 3 by setting $D^*=0$. For simplicity in comparisons to the PTW model below, let p=q=m=1. Equation 3 can then be inverted to isolate the thermal component of the normalized flow stress, $\hat{\sigma}_T = \sigma_T/G$, namely

$$\hat{\sigma}_T = \frac{\sigma_A}{G_0} + \frac{\sigma_P}{G_0} - \frac{\sigma_P}{G_0}\frac{kT}{2U_k}\ln\left(\frac{\dot{\varepsilon}_0}{\dot{\varepsilon}}\right), \quad (4)$$

where $\dot{\varepsilon}_0 = \alpha \nu_{De} \rho_m b^2$, $1/\alpha = 2w^2/La$, with w, L, and a as defined in [7,9].

We wish to compare Eq. 4 with the PTW model, [11] which we write here in a simplified form, assuming $\varepsilon \approx 0$ (low strain, negligible work hardening), namely

$$\hat{\tau} = \max\left\{ y_0 - (y_0 - y_\infty)\,\mathrm{erf}\left[\kappa \hat{T} \ln\left(\frac{\gamma\dot{\xi}}{\dot{\varepsilon}}\right)\right], s_0\left(\frac{\dot{\varepsilon}}{\gamma\dot{\xi}}\right)^\beta \right\} \quad (5)$$

Here, y_0 represents the total flow stress at T = 0 (ie, the sum of the athermal baseline plus Peierls stress). The parameter y_∞ corresponds to flow stress at high temperature, where $\mathrm{erf}(x) \approx 1$, where flow stress is no longer sensitive to temperature, at least in terms of surmounting barriers. The parameter, $\dot{\xi} = c_{sh}/2a \sim \omega_{De}$, is a reference strain rate, where c_{sh} is the shear wave speed, $4\pi a^3/3$ is the atomic volume, and ω_{De} the Debye frequency. [11] If we consider only the thermal activation component, and limit the discussion to the linear region of the error function, where $\mathrm{erf}(x) \approx (2/\sqrt{\pi})x$, we can approximate the scaled flow stress as

$$\hat{\tau} \approx y_0 - \frac{2}{\sqrt{\pi}}(y_0 - y_\infty)\kappa \hat{T} \ln\left(\frac{\gamma\dot{\xi}}{\dot{\varepsilon}}\right). \quad (6)$$

By comparing like terms in Equations 4 and 6, we can correlate the PTW "free parameters" γ, κ, y_∞, and y_0 with physical quantities from the H-M* model, giving $\gamma \sim \rho_m b^2$, $\kappa \sim 1/U_k$, $y_\infty \sim \hat{\sigma}_A$, $y_0 \sim \hat{\sigma}_A + \hat{\sigma}_P$, and $y_0 - y_\infty \sim \hat{\sigma}_P$.

The correlation $\gamma \sim \rho_m b^2$ is particularly interesting. [Note, an analysis of the phonon drag components of Eqs. 3 and 5 leads to a similar result, provided that $m=1/\beta$.] If the mobile dislocation density, ρ_m, depends on the dynamics of the system, as suggested by recent molecular dynamics (MD) simulations of shocked Cu, [12] then γ may also depend on the dynamics. This discussion also applies to the S-L (Eq. 2) and the H-M (Eq. 3) models, which also treat ρ_m as a material constant, when it may be a dynamically evolving variable. Developing a theoretical approach to follow the evolution of $\rho_m(t)$ is a difficult endeavor, but may be required. Very large scale MD simulations, [12] or the new technique of multiscale dislocation dynamics plasticity [13] may be beneficial in this task.

The last model we discuss is the Zerilli-Armstrong model. [14-16] We consider the version described for Ta, [15] which is written as

$$\sigma = c_0 + K\varepsilon^n + B_0 e^{-\beta T}, \qquad (7)$$

where $c_0 = \sigma_G + k\ell^{-1/2}$, and $\beta = \beta_0 - \beta_1 \ln\dot{\varepsilon}$. Here, σ_G, ℓ, β_0, and β_1 correspond to the athermal stress due to the initial defect density, grain size, and material constants, resp. The form of the thermal activation term, $B_0 e^{-\beta T}$, was motivated originally by the data of Heslop and Petch, which showed that the temperature dependent portion of the flow stress decreased as T increased. [17,18], that is, $d\sigma/dT < 0$. At the strain rates where this model has been traditionally applied, $\beta = \beta_0 - \beta_1 \ln\dot{\varepsilon} > 0$, so that automatically $d\sigma/dT < 0$. At the very high strain rates considered here, however, this may not always be true. So we explicitly require that $\beta > 0$, which implies that the model is applicable for strain rates $\dot{\varepsilon} < e^{\beta_0/\beta_1}$. We also need to include pressure hardening, which we accomplish with an overall G/G_0 multiplier. Hence, our modified Zerilli-Armstrong model ($Z\text{-}A_1$), applicable for $\dot{\varepsilon} < e^{\beta_0/\beta_1}$, is written as

$$\sigma = \left[c_0 + K\varepsilon^n + Be^{-(\beta_0 - \beta_1 \ln\dot{\varepsilon})T}\right]\frac{G(P,T)}{G_0}. \qquad (8)$$

Note, for $\beta_0 >> \beta_1 \ln\dot{\varepsilon}$, the $Z\text{-}A_1$ strength in Eq. 8 becomes independent of strain rate, similar to the first term in Eq. 6 or the first two terms of Eq. 4. At very high strain rates, $\beta = \beta_0 - \beta_1 \ln\dot{\varepsilon}$ becomes small, and a first order Taylor expansion of the exponential in Eq. 8 leads to $\sigma \propto \ln\dot{\varepsilon}$, similar to the last terms of Eqs. 4 and 6. Hence, there is nice consistency between the models, over the ranges where they are mutually applicable.

We illustrate the models discussed above in Fig. 1 as a function of strain rate, for Ta at P = 0.5 Mbar, T = 500 K, and $\varepsilon = 0.1$. The dot-dashed curve labeled ($S\text{-}L_0$) corresponds to the nominal S-L model (Eq. 2a, including the S-L cap on σ_T when $\sigma_T > \sigma_P$) with nominal input parameters for Ta. [9] The dashed curve labeled ($S\text{-}L_1$) corresponds to the S-L model with the artificial cap on σ_T removed. Curves ($S\text{-}L_1$) and ($S\text{-}L_0$) coincide in the thermal activation regime, for $\dot{\varepsilon} < 10^5$ s^{-1}. At higher strain rates, $\dot{\varepsilon} > \sim 10^6$ s^{-1}, the nominal S-L model, curve ($S\text{-}L_0$), transitions to essentially the Steinberg-Guinan model, Eq. 1, which is strain rate

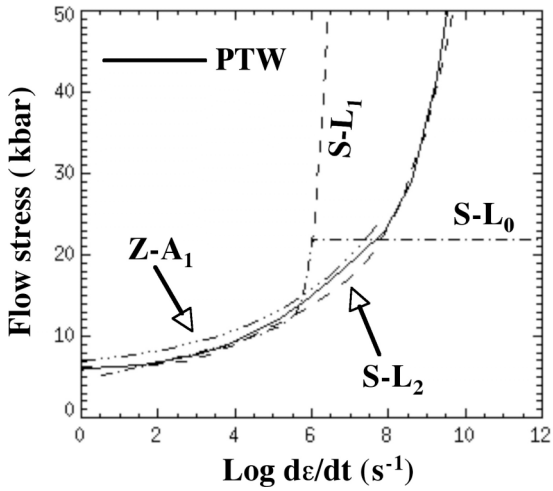

FIGURE 1. Flow stress (kbar) versus log strain rate for a variety of constitutive models (see text for details) for Ta at 0.5 Mbar, 500 K temperature, and plastic strain of 0.1. The nominal Steinberg-Lund model is the curve labeled $S\text{-}L_0$. Steinberg-Lund, with the artificial cap on σ_T removed, is shown by the curve labeled $S\text{-}L_1$. Steinberg-Lund, modified to resemble PTW, is shown by the curve labeled $S\text{-}L_2$. The nominal PTW model is shown by the solid curve. And a slightly refined Zerilli-Armstrong model, suitable for these high pressures and strain rates, is shown by the curve labeled $Z\text{-}A_1$.

independent. Note, for the $S\text{-}L_1$ model at high strain rates, where phonon drag dominates flow stress, as shown by curve ($S\text{-}L_1$) in Fig. 1, $\sigma_T >> \sigma_A f(\varepsilon)$ in Eq. 2a, and strength is predicted to be essentially independent of the initial microstructure and work hardening. The solid curve labeled (PTW) in Fig. 1 corresponds to the PTW model, Eq. 5, with nominal input parameters for Ta. [11] In the low strain rate regime, $\dot{\varepsilon} < \sim 10^5$ s^{-1}, PTW also agrees with the S-L models. This is not surprising, since both models were "calibrated" against similar Hopkinson bar data. With nominal input parameters for Ta, the PTW model transitions to phonon drag at a higher strain rate, $\sim 10^8$ s^{-1}, due to the higher reference strain rate $\dot{\xi}$ (~ attempt frequency), than the S-L models. The transition is

to a power-law "nonlinear" phonon drag model, with a softer dependence on strain rate, $\sigma \propto \dot{\varepsilon}^{1/4}$, based on overdriven shock data. The S-L_2 model (Eqs. 3 + 2a, with m=4, p=1, q=2, and no cap on σ_T) is shown in Fig. 1 by the dashed curve (S-L_2). Here, the reference strain rate (~ attempt frequency), $\dot{\varepsilon}_0$, has been increased by ~100x over the nominal value. Under these settings, the S-L_2 model is consistent with the PTW model over essentially the entire strain rate range.

Finally, we show in Fig. 1 the results of the modified Zerilli-Armstrong model (Eq. 8) by the multidot-dashed curve labeled Z-A_1. For nominal input parameters for this model for Ta, the thermal activation regime extends to the low x 10^7 s^{-1} strain rate regime, and over this range, it agrees very well with the PTW model. As described in [14,15] this model addresses deformation in the thermal activation regime. Zerilli and Armstrong pointed out nearly two decades ago, however, that to extend to higher strain rates one should address the increase of dislocation density, as opposed to treating ρ_m as a material constant. [14] This is a key point, which we also mention in the discussion below Eq. 6, which remains to be addressed in future constitutive models addressing high strain rate deformation. In summary, all the models essentially agree, with reasonable parameter settings, in the thermal activation regime. At the highest strain rates, where thermal activation no longer applies, the models diverge significantly. New data will be needed to test the models in this ultrahigh strain rate regime.

RAYLEIGH-TAYLOR STRENGTH METHOD

We next discuss a technique for generating a ramped "drive" to load samples to high pressure in the solid state for testing models of material strength. The drive technique has been experimentally demonstrated up to peak pressures of 200 GPa (2 Mbar) at the Omega laser, as shown in Fig. 3. [19] The target typically consists of a solid density plastic reservoir of nominal thickness ~0.2 mm, followed by a ~0.3 mm vacuum gap, then an Al sample. A laser pulse of energy 0.2 – 2 kJ in a temporally square pulse shape of duration 3 – 4 ns is used to drive a strong shock through the low-Z reservoir. When the shock reaches the back side, the reservoir unloads into vacuum as a plasma "ejecta". The pressure that is applied to the sample

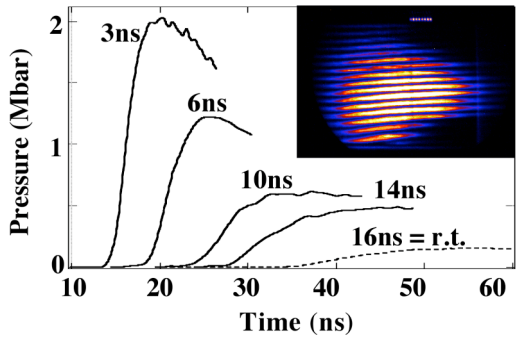

FIGURE 2. Pressure vs. time for five different experiments, showing the ramped drive for maximum pressures spanning 0.15 kbar to 2 Mbar. [19]

results from the ram pressure, $P_{ram} = \rho_{ejecta} v^2_{ejecta}$, due to the inflowing ejecta. This increases smoothly and monotonically in time as the reservoir unloads. We modeled this shockless compression technique after the early work of Barnes using high explosives (HE) as the source of the shock in the reservoir. [20,21] The measured velocity profiles can be back integrated to infer the applied pressure vs. time at the front surface of the Al sample, using a technique developed by Hayes. [4] We show in Fig. 2 the results from five different experiments, varying mainly the laser intensity, leading to peak pressures spanning 0.15 – 2 Mbar. As the peak pressure increases, the rise time decreases. At 2 Mbar, with a ~3 ns rise time, the sample is not shocked, at least over the first 10-20 μm of Al. Furthermore, design simulations show that on future facilities, such as the NIF laser, [6] this technique should be able to drive samples in the solid state to much higher pressures, P > 10 Mbar. [22]

We show in Fig. 3 the results of 2D simulations of the Rayleigh-Taylor (RT) instability, [23] for a quasi-isentropically driven RT experiment in Ta at P_{max} ~ 2 Mbar. This experiment was designed for the first bundle of the NIF laser. [6] The simulations assumed the S-G strength model, and varied the initial strength parameter, σ_0. There is considerable sensitivity in the predicted RT growth factors, due to the

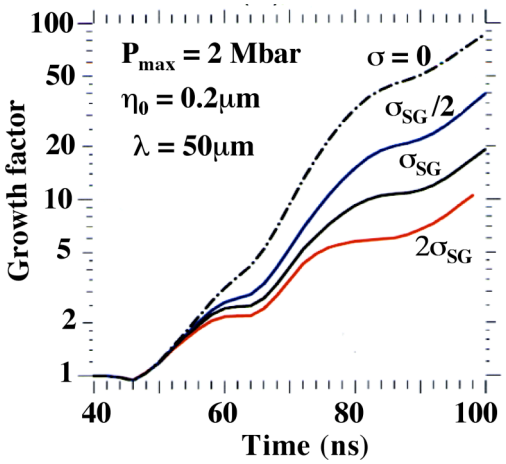

FIGURE 3. Growth factor vs time (ns). Predicted RT growth of preimposed sinusoidal ripple (wavelength λ = 50 μm, initial amplitude η_0 = 0.2 μm) showing sensitivity to high pressure strength for Ta at 2 Mbar peak pressure. Note the log scale.

stabilizing influence of material strength. Recent experiments on Omega in V and Al at lower peak pressures corroborate this prediction. [23]

LATTICE DIAGNOSTICS

We conclude by summarizing a selection from our work at the lattice level, starting with dynamic diffraction experiments. [24] This technique offers the potential to probe fundamental quantities such as phase, Peierls barrier, and dislocation mobility, at high pressures and strain rates, and is particularly well suited to studies of shocked, single crystals. We show an example from a dynamic (driven) experiment in Fig. 4 for single crystal Ti shocked along the [0001] direction at P_{shk} ~ 70 kbar, done on the Janus laser at LLNL. [25] One laser beam is used to shock the crystal, while a second beam, the "backlighter", is used to drive a point source of x-rays, located to match the Bragg diffraction condition, $2d \sin\theta = n\lambda$, where d is the lattice spacing, n is the order, and λ is the x-ray wavelength. Initially there is diffraction only from the unshocked region (lower arc, labeled "ambient"). Later in time, the Ti has been shocked. With the backlighter laser double pulsed, both shocked and unshocked regions can be superposed on the same film pack, as shown in the image in Fig. 4. The diffraction experiments give the phase and lattice compression, and can probe whether the lattice is in a plastically relaxed 3D state (~hydrostatic), or a uniaxially compressed 1D state. [12, 24]

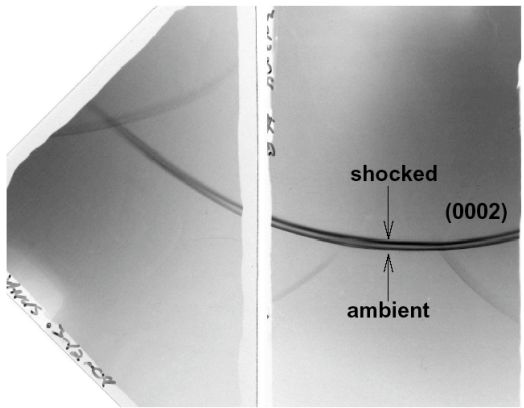

Figure 4. Example of the dynamic diffraction technique for shocked single crystal Ti, at P_{shk} ~ 70 kbar, shocked along the [0001] direction. [25]

We have also developed the time-resolved EXAFS diagnostic technique at the Omega laser. [26] Three laser beams are used to shock compress the sample being studied. The remaining 57 beams implode an inertial confinement fusion capsule to generate a short (~120 ps) burst of smoothly varying hard x-rays, $I = I_0 \exp(-E_x/T)$, to be used for the EXAFS absorption. We show the result for shocked polycrystalline Ti at $P_{shk} \approx 330$ kbar in Fig. 5. [26] The modulations as a function of electron energy, or equivalently, electron wave number, are due to the interference from reflections off neighboring atoms, that occur as the freed electron (from bound-free x-ray absorption) leaves its host atom. These modulations can be modeled with an EXAFS theoretical model (FEFF8) to infer lattice compression, phase, and temperature. In Fig. 5, if we assume that the shock temperature is the same as for shocked V experiments at the same shock strength, which agree with LASNEX radiation-hydrodynamics simulations, then fit the FEFF8 model to reproduce the modulation period, assuming no phase transition, the result is shown in green, labeled α-Ti. The fit is clearly unsatisfactory, and suggests this interpretation

cannot be correct. If we again assume no phase transition, but arbitrarily increase the temperature until the theoretical curve fits the data, the resulting

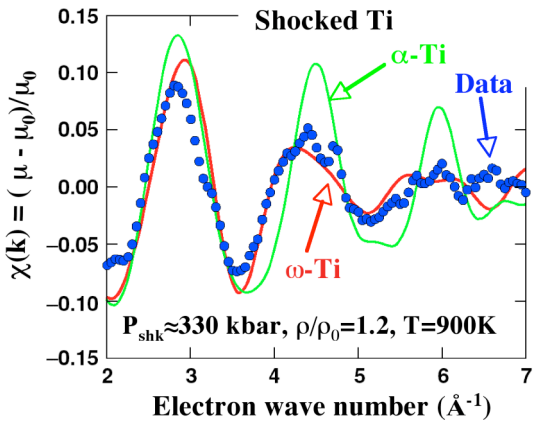

Figure 5. Dynamic EXAFS measurements of shocked Ti at P_{shk} = 330 kbar (33 GPa). [26]

temperature is T≈2100 K. This temperature is over a factor of two higher than predicted with simulations, and in distinct disagreement with temperatures inferred from shocked V experiments at the same shock strength. If, on the other hand, the shocked Ti has undergone the α–ω phase transition, as expected for these pressures, and we assume the shock temperatures from the radiation-hydrodynamics simulations of T≈900 K, the result is shown by the red curve in Fig. 5, labeled ω-Ti. The agreement with the data is excellent, and suggests that this is the most likely interpretation. At P_{shk} ≈ 330 kbar, the time scale for the α–ω phase transition in Ti is prompt, $\delta t_{\alpha-\varepsilon}$ < 1 nsec.

CONCLUSION

We are developing the capability to do solid state, material dynamics experiments at very high pressures and strain rates (P, $\dot{\varepsilon}$), where model uncertainties are very large. A ramped pressure drive has been developed to reach high – (P, $\dot{\varepsilon}$) in the solid state, and Rayleigh-Taylor experiment designs show sensitivity to the strength models in this regime. Dynamic diffraction measures lattice response, compression and phase, and dynamic EXAFS independently measures compression, phase, and temperature, all relevant to testing constitutive models. Phase transitions have been inferred with transition time scales < ~1 nsec.

ACKNOWLEDGEMENTS

*This work was performed under the auspices of the U.S. Department of Energy by the Lawrence Livermore National Laboratory under Contract No. W-7405-ENG-48. We are grateful for many illuminating discussions with D. Preston.

REFERENCES

1. Remington, B.A. et al., Met. Mat. Trans. 35A, 2587, 2004.
2. Remington, B.A. et al., submitted, MST, 2005
3. Reisman, D.B. et al., J. Appl. Physics 89, 1625, 2001.
4. Hayes, D. B. et al., J. Appl. Phys. 96, 5520, 2004.
5. Huang, H. and Asay, J.R., J. Appl. Phys. 98, 033524, 2005.
6. Hogan, W.J. et al., et al., Nuclear Fusion 41, 567, 2001.
7. Hoge, K.G. and Mukherjee, A.K., J. Mat. Sci. 12, 1666, 1977.
8. Steinberg, D.J., Cochran, S.G., and Guinan, M.W., J. Appl. Phys. 51, 1496, 1980.
9. Steinberg, D.J. and Lund, C.M., J. Appl. Phys. 65, 1528, 1989.
10. Zerilli, F.J. and Armstrong, R.W., Acta Metall. Mater. 40, p. 1803, 1992.
11. Preston, D.L., Tonks, D.L., and Wallace, D.C., J. Appl. Phys. 93, 211, 2003.
12. Bringa, E.M. et al., Nature Mat., submitted, 2005.
13. Zbib, H.M. and Diaz de la Rubia, T., Int. J. Plasticity 18, 1133, 2002.
14. Zerilli, F.J. and Armstrong, R.W., J. Appl. Phys. 61, 1816, 1987.
15. Zerilli, F.J. and Armstrong, R.W., J. Appl. Phys. 68, 1580, 1990.
16. Petch, N.J., Phil. Mag. 3, 1089, 1958.
17. Heslop, J. and Petch, N.J., Phil. Mag. 1, 866, 1956.
18. Heslop, J. and Petch, N.J., Phil. Mag. 3, 1128, 1958.
19. Edwards, J. et al., Phys. Rev. Lett. 92, 075002, 2004.
20. Barnes, J.F. et al., J. App. Phys. 45, 727, 1974.
21. Barnes, J.F. et al., J. Appl. Phys. 51, 4678, 1980.
22. Remington, B.A. et al., Astrophys. Space Science 298, 235, 2005.
23. Lorenz, K.T. et al., Phys. Plasmas, 12, 056309, 2005.
24. Loveridge-Smith, A. et al., Phys. Rev. Lett., 86, 2349, 2001.
25. Swift, D.C. et al., Phys. Plasmas 12, 056308, 2005.
26. Yaakobi, B. et al., Phys. Plasmas, 11, 2688, 2004.